Spin Filter for Polarized Electron Acceleration in Plasma Wakefields

Yitong Wu,[1,2] Liangliang Ji,[1,3,*] Xuesong Geng,[1,2] Johannes Thomas,[4] Markus Büscher,[5,6] Alexander Pukhov,[4] Anna Hützen,[5,6] Lingang Zhang,[1] Baifei Shen,[1,3,7,†] and Ruxin Li[1,3,8,‡]

[1] *State Key Laboratory of High Field Laser Physics, Shanghai Institute of Optics and Fine Mechanics, Chinese Academy of Sciences, 201800 Shanghai, China*

[2] *Center of Materials Science and Optoelectronics Engineering, University of Chinese Academy of Sciences, 100049 Beijing, China*

[3] *CAS Center for Excellence in Ultra-intense Laser Science, 201800 Shanghai, China*

[4] *Institut für Theoretische Physik I, Heinrich-Heine-Universität Düsseldorf, Universitätsstraße 1, 40225 Düsseldorf, Germany*

[5] *Peter Grünberg Institut (PGI-6), Forschungszentrum Jülich, Wilhelm-Johnen-Straße 1, 52425 Jülich, Germany*

[6] *Institut für Laser- und Plasmaphysik, Heinrich-Heine-Universität Düsseldorf, Universitätsstraße 1, 40225 Düsseldorf, Germany*

[7] *Shanghai Normal University, 200234 Shanghai, China*

[8] *Shanghai Tech University, 201210 Shanghai, China*

(Received 15 December 2019; accepted 31 March 2020; published 24 April 2020)

We propose a filter method to generate electron beams of high polarization from bubble and blow-out wakefield accelerators. The mechanism is based on the idea of identifying all electron-beam subsets with low polarization and filtering them out with an X-shaped slit placed immediately behind the plasma accelerator. To find these subsets we investigate the dependence between the initial azimuthal angle and the spin of single electrons during the trapping process. This dependence shows that transverse electron spins preserve their orientation during injection if they are initially aligned parallel or antiparallel to the local magnetic field. We derive a precise correlation of the local beam polarization as a function of the coordinate and the electron phase angle. Three-dimensional particle-in-cell simulations, incorporating classical spin dynamics, show that the beam polarization can be increased from 35% to about 80% after spin filtering. The injected flux is strongly restricted to preserve the beam polarization; for example, less than 1 kA in Wen *et al.* [Phys. Rev. Lett. 122, 214801 (2019)]. This limitation is removed by use of the proposed filter mechanism. The robustness of the method is discussed in terms of drive-beam fluctuations, jitters, the thickness of the filter, and the initial temperature. This idea marks an efficient and simple strategy to generate energetic polarized electron beams on the basis of wakefield acceleration.

DOI: 10.1103/PhysRevApplied.13.044064

I. INTRODUCTION

Wakefield acceleration driven by either laser pulses [laser wakefield acceleration (LWFA)] [1] or electron beams [plasma wakefield acceleration (PWFA)] [2] is advantageous due to its large acceleration gradient, reaching almost gigaelectronvolts per centimeter [3], which is about 3 orders of magnitude higher than traditional accelerators [4]. The generation of gigaelectronvolt-level electron beams from both LWFA [5–7] and PWFA [8–10] was realized recently, among which electron energy of 8 GeV is obtained via LWFA [6] and several gigaelectronvolts is obtained via PWFA [9,10]. These results pave a path to toward tabletop accelerators and secondary light sources. An ultimate goal of wakefield acceleration is the pursuit of future electron-positron colliders [11,12]. Particularly, spin-polarized electron and positron beams are favorable for the colliders. There are at least three main advantages of applying polarized beams: (i) the cross section is enhanced for certain reaction processes [13–16]; (ii) unwanted background processes and reaction channels can be suppressed with appropriate combinations of the electron-beam and positron-beam polarizations [14,15]; (iii) by choosing suitable observables in the scattering processes, one can obtain additional information, such as quantum numbers and chiral couplings [14,16].

*jill@siom.ac.cn
†bfshen@mail.shcnc.ac.cn
‡ruxinli@mail.siom.ac.cn

Furthermore, energetic polarized electron beams are also used to generate polarized photons [17] and positrons [18] as well as to study material properties and nuclear physics [19–21].

Conventionally, high-energy polarized electron beams are obtained either from storage rings [19,20] based on radiative polarization (the Sokolov-Ternov effect [22], similar effects obtained with ultraintense lasers are reported in Ref. [23]) or by extracting polarized electrons directly (via photocathodes [21,24], spin filters [21, 25], or beam splitters [21,26]) for subsequent acceleration in linacs. Recently polarized electron generation based on plasma wakefields was explored in simulations [27–29]. The idea includes preparation of prepolarized targets via the photodissociation of hydrogen halides [30–34]. The prepolarized electrons suffer from depolarization in a plasma wakefield due to the spin precession in the self-generated magnetic field associated with the injected electrons. To preserve the electron polarization during the entire acceleration process, strong limitations must be imposed on the beam parameters, the plasma density, and the injected-beam flux. This can be mitigated by either restricting the electron flux to less than 1 kA at laser amplitudes $a < 1.1$ as proposed in Ref. [27] or by use of vortex wakefield structures [28].

In this paper, we propose a filter mechanism by selecting targeted electrons out of the whole accelerated beam to achieve polarization greater than 80%. The mechanism largely removes the flux-limitation issue on injected electrons. It relies on the fact that the beam polarization is dependent on the spatial and momentum angles—a universal phenomenon in density down-ramp injection. Specifically, in particle-in-cell (PIC) simulations incorporating spin dynamics we show that spin precession in a wakefield is significantly suppressed when the initial spin is parallel or antiparallel to the local azimuthal magnetic field, leading to dependence of the beam polarization on the transverse coordinate angle in the plasma bubble. We then propose selecting electrons from the related region in the transverse phase space with an X-shaped slit, which successfully maximizes the polarization of the accelerated beam. This unique feature applies to transverse polarization.

II. SIMULATION METHODS AND SETUPS

To demonstrate the spin-filter mechanism, perform full three-dimensional (3D) PIC simulations with the code VLPL (Virtual Laser Plasma Lab) [35]. To investigate spin dynamics, we integrate the spin precession into the PIC code following the Thomas-Bargmann-Michel-Telegdi equation [36]:

$$d\mathbf{s}/dt = \mathbf{\Omega} \times \mathbf{s} \tag{1a}$$

$$\mathbf{\Omega} = \frac{e}{m}\left(\frac{1}{\gamma}\mathbf{B} - \frac{\boldsymbol{\beta}}{\gamma+1}\times\frac{\mathbf{E}}{c}\right) + a_e\frac{e}{m}\left(\mathbf{B} - \frac{\gamma}{\gamma+1}\boldsymbol{\beta}(\boldsymbol{\beta}\cdot\mathbf{B}) - \boldsymbol{\beta}\times\frac{\mathbf{E}}{c}\right), \tag{1b}$$

where e is the elementary charge, m is the electron mass, $\boldsymbol{\beta} = \mathbf{v}/c$ is the normalized electron velocity, $\gamma = 1/(1-v^2/c^2)^{1/2}$ is the relativistic factor, $\mathbf{s}$ represents the normalized particle spin-direction vector, with $|\mathbf{s}| = 1$ following Ehrenfest's theorem [19], $a_e = (g-2)/2 \approx 1.16\times10^{-3}$ (gyromagnetic factor g), and the vector $\mathbf{\Omega}$ is the precession frequency. As mentioned in Refs. [27–29], other effects, such as the Stern-Gerlach force (gradient force), the Sokolov-Ternov effect (radiative polarization) [22], and electrostatic Coulomb collisions [37,38], are negligibly small for wakefield acceleration. Comparison of the Stern-Gerlach force with the Lorentz force of wakefield acceleration $|F_{\mathrm{S\text{-}G}}/F_{\mathrm{L}}| \sim |\nabla(\mathbf{S}\cdot\mathbf{B})/{\gamma_e}^2 c\mathbf{B}m_e| \sim \hbar/\lambda m_e c{\gamma_e}^2 \sim 10^{-7}$ [19,28] suggests the drift motion caused by such a force is small enough to be ignored. With regard to the Sokolov-Ternov effect, the typical polarization time $T_{\mathrm{pol,S\text{-}T}}$ is about $8{m_e}^5c^8/5\sqrt{3}\hbar e^5F^3{\gamma_e}^2$ [19,28]. For typical wakefield acceleration ($\gamma_{\mathrm{e}} \sim 10^3$ and field strength $F \sim 10^{16}$ V/m), one has $T_{\mathrm{pol,S-T}} \approx 1$ μs, corresponding to an acceleration distance of about 300 m, which is much larger than the typical wakefield acceleration distance.

In all the simulations, to ensure high injection efficiency [39–41], a transversely prepolarized target (along the $+z$ axis) with a density bump is assumed. According to previous work [27–29], such a plasma density is usually parametrized by a ramp-shaped profile, $n(\kappa) = \{[\alpha - \Theta(\kappa)]\Theta(L-\kappa)\cos(\pi\kappa/2L) + \Theta(\kappa-L)\}n_0$, where $\Theta(x)$ is the step function, $\kappa = x - x_p$ ($x_p = 36$ μm), $L = 16$ μm, $n_0 = 10^{18}$ cm^{-3}, and $\alpha = n_p/n_0 = 4$ is the ratio between the peak density of the ramp and the background density. The driver beam (laser or particles) propagates into a moving window of size 48 μm (x) × 48 μm (y) × 48 μm (z) size and cell number of 1200 × 480 × 480 with six macroparticles in each cell. The laser beam is linearly polarized along the y axis, following a Gaussian profile, $E_L = a{w_0}^2/w^2(x)\sin^2(\pi t/2\tau_0)\sin(\pi r^2/\lambda R)\exp[-r^2/w^2(x)]$, with normalized peak amplitude $a = eE/m\omega c$, $r^2 = y^2 + z^2$, wavelength $\lambda = 800$ nm, $w(x) = w_0\{[(x-x_p)^2 + {x_R}^2]/{x_R}^2\}^{1/2}$, $R = (x^2 + {x_R}^2)/x$, Rayleigh length $x_R = \pi {w_0}^2/\lambda$, width $w_0 = 10\lambda = 8$ μm, and duration $\tau_0 = 10\lambda/c = 26.7$ fs. The electron driver beam also takes a Gaussian profile [8] $n_b(r,\xi = x - ct) = n_{b0}\exp(-r^2/2{\sigma_r}^2 - \xi^2/2{\sigma_l}^2)$, where σ_l and σ_r are the longitudinal and transverse beam sizes and $n_{b0} = 1.5\times10^{19}$ cm^{-3} denotes the peak density of the driving beam. The simulation time step $\Delta t = 0.01\lambda/c$, ensuring that the largest precession angle in each time step $|\theta_{s,\max}| = \Omega_{\max}\Delta t \sim 0.02\pi B_{\max}$ (B is normalized by $m\omega/e$) is sufficiently small ($|\theta_{s,\max}| \ll 2\pi$).

III. RESULTS

The electron-density distributions of a typical LWFA and the corresponding transverse fields based on density down-ramp injection are displayed in Fig. 1(a). The results are collected for $a = 2.5$, $\alpha = 4$, and $n_0 = 10^{18}\,\mathrm{cm}^{-3}$. A spherelike bubble is generated by the laser ponderomotive force. The injected electrons are located at the rear of the bubble and continuously gain energy from the longitudinal field. The total charge of the injected beam is about 62 nC and peak current reaches 9.2 kA. Seen from the directional arrows in the transverse y-z plane, we notice that the transverse fields satisfy $\mathbf{B}_T \approx -B_\phi \mathbf{e}_\phi$ and $\mathbf{E}_T \approx E_r \mathbf{e}_r$. Such field distributions indicate a central force on the injected electrons. We show the trajectories of electrons initially located at radius $|r_i| = 6.4\ \mu$m in Fig. 1(b) and mark their spin orientations during the injection phase for selected electrons at distinct coordinate angles $\phi = \tan^{-1}(z/y)$ in the range from $-\pi/2$ to $\pi/2$ (since $\phi + \pi$ and ϕ correspond to the same axis with opposite directions, it suffices to treat the region $\phi \in [-\pi/2, \pi/2]$). It is seen that due to the cylinder symmetry of the bubble forces, all electrons are focused to the center, following almost identical trajectories about the central axis. However, the spin precessions are different for electrons of different ϕ. In particular, the electron spin is preserved at $\phi = 0$ (along the y axis) during injection, while it changes dramatically for $\phi = \pm\pi/2$ (along the z axis).

The trajectories basically remain in a plane defined by the coordinates and the central axis for each electron. This indicates that the azimuthal angle is the same in both the coordinate space (ϕ) and the transverse phase space [defined as $\phi_p = \tan^{-1}(P_z/P_y)$] during the injection. For instance, the electrons located at ϕ in the range $[-\pi/2, \pi/2]$ would be directed along $\phi_p \sim [-\pi/2, \pi/2]$ in the

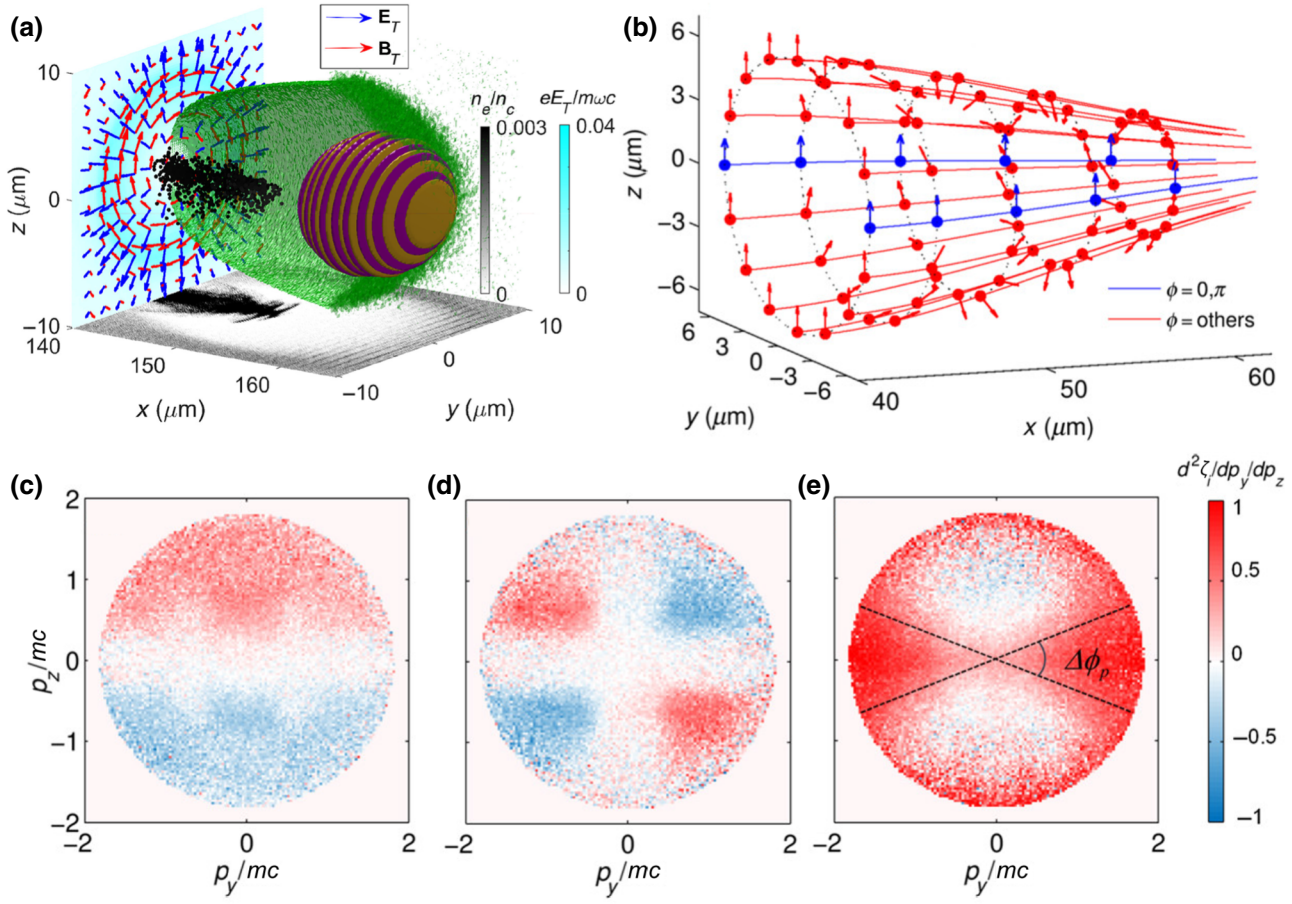

FIG. 1. (a) A typical LWFA structure and transverse-field distributions, with the bubble (green surface), the laser beam (yellow-purple isosurfaces for $|E_y| = 1.5$), the injected electrons (black dots), the electron density (the x-y plane), and the transverse electric field ($\mathbf{E}_T$, blue arrows) and transverse magnetic field ($\mathbf{B}_T$, red arrows). The amplitude of $\mathbf{E}_T = (E_y{}^2 + E_z{}^2)^{1/2}$ ($x = 150\ \mu$m plane) is projected onto the $x = 140\ \mu$m plane. (b) Electron trajectories (solid lines) and spin orientations (arrows) during injection with $\phi \in [-\pi/2, \pi/2]$ at injection radius $|r_i| = 6.4\ \mu$m, with $\phi = 0$ marked in blue and the rest in red. The polarization (average spin components in mesh grids) distributions in the transverse phase space (p_y-p_z) [(c)–(e), respectively] along the x, y, and z axes at 800 fs. The results are collected for simulation parameters $a = 2.5$, $\alpha = 4$, and $n_0 = 10^{18}\,\mathrm{cm}^{-3}$ and initial electron spins are set along the z axis. The cross-shaped area defined by the phase angle $\Delta\phi_p$ in (e) represents the high-polarization region.

transverse directions. Therefore, spins should be preserved for electrons moving close to the y axis ($|p_z| \ll |p_y|$) and change significantly around the z axis ($|p_z| \gg |p_y|$). To further prove this statement, we give the polarization $\Sigma s_i/N$ distributions in p_y-p_z space along the x, y, and z axes (averaging the corresponding spin components in p_y-p_z mesh grids). As illustrated in Fig. 1(e) for beam polarization along the $+z$ axis (the initial spin orientation), the polarization purity peaks in the vicinity of $\phi_p \sim 0$ and vanishes otherwise, exhibiting a saddlelike distribution. The polarization along the y axis in Fig. 1(d) is also centrally symmetric but peaks at $\phi_p \approx \pm\pi/4$ (where $|p_z| \approx |p_y|$). The polarization along the x axis is symmetric about the $p_z = 0$ axis and averaged out at specific ϕ_p as shown in Fig. 1(c). Simulations suggest that the peak value of the polarization along the z axis is well retained at more than 80% among the cross region of $|\phi_p| < \pi/4$, which allows spin filtering in the transverse phase space.

To explain the above observations, we consider a quasistatic scenario, where the bubble fields are cylinder symmetric; that is, where $\mathbf{B} \approx -B_\phi \mathbf{e}_\phi$, $\beta \approx \beta_x$, and $\boldsymbol{\beta} \times \mathbf{E} \approx E_r \beta_x \mathbf{e}_\phi$ [42–44]. Such field distributions are also seen in our simulations [Fig. 1(a)]. As stated in previous work [27–29,45], the spin is preserved during steady acceleration but precesses dramatically during the injection phase. That is why we focus on the spin dynamics during injection, where typically one has $\gamma \ll 1/a_e$ [42,46] and the second term of Eq. (1b) can be ignored. With these simplifications, the precession frequency $\boldsymbol{\Omega}$ and the equation of motion in the transverse direction can be written as

$$\boldsymbol{\Omega} = -\frac{e}{m}\left(\frac{B_\phi}{\gamma} + \frac{\beta_x}{\gamma+1}\frac{E_r}{c}\right)\mathbf{e}_\phi, \tag{2}$$

$$mc\frac{\partial}{\partial t}\mathbf{P}_T = e(E_r + c\beta_x B_\phi)\mathbf{e}_r = F_r \mathbf{e}_r. \tag{3}$$

An obvious effect revealed by Eq. (3) is that the electrons feel radial forces only in transverse directions $\partial \mathbf{P}_T/\partial t \approx \partial \mathbf{P}_r/\partial t$. Since electrons injected at an azimuthal angle ϕ carry zero initial azimuthal momentum (i.e., $\mathbf{P}_\phi \approx 0$), the azimuthal angles are equivalent in the coordinate space and the phase space $\phi \approx \phi_p$ during the whole injection process, which agrees with the trajectories in Fig. 1(b). The distributions of injected electrons with their transverse-momentum vectors in Fig. 2(a) further demonstrate that momentum vectors are almost parallel to the coordinate vector direction, with negligible minor discrepancies. The difference between the two defined by ϕ–ϕ_p is counted over all injected electrons, which shows a root-mean-square value of only 0.063π in Fig. 2(b).

From Eq. (3), the coordinate angle ϕ of an electron is always fixed (there is no lateral force perpendicular to $\mathbf{e}_r$) which guarantees that the precession axis is stationary (along $\mathbf{e}_\phi$). The precession angle satisfies $\Delta\theta_s = \langle\boldsymbol{\Omega}\rangle \Delta T$, where $\Delta T \approx 4|r_i|/c$ is the injection time, where r_i is the injection radius [47–49]. The spin vector after injection (starting at $t = t_0$) can then be deduced from $\mathbf{s}(t_0 + \Delta T) = \mathbf{s}_\parallel(t_0 + \Delta T) + \mathbf{s}_\perp(t_0 + \Delta T) = \mathbf{s}_\parallel(t_0) + \cos(\Delta\theta_s)\mathbf{s}_\perp(t_0) + \sin(\Delta\theta_s)\mathbf{e}_\phi \times \mathbf{s}_\perp(t_0)$, where $\mathbf{s}_\parallel(t_0) =$

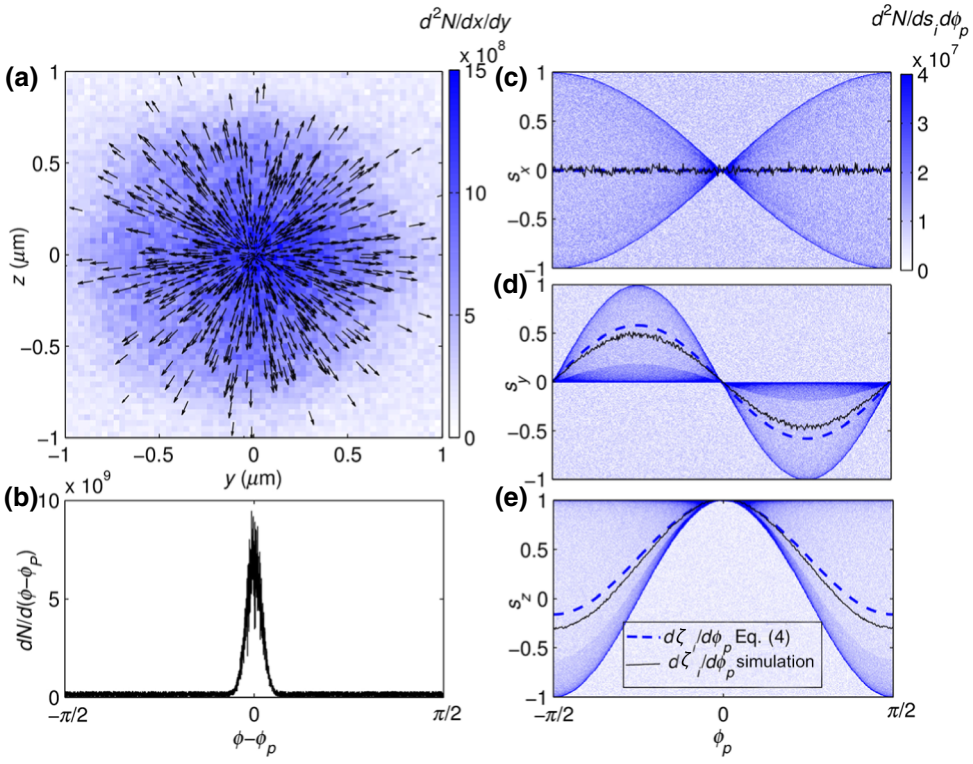

FIG. 2. Number density in the y-z plane (a) and $\phi-\phi_p$ (b) of all injected electrons. The black arrows in (a) denote transverse momentum-vector directions for 1000 randomly selected electrons. (a)–(c) The particle densities in the ϕ_p-s_i space, where $i = x$ (c), $i = y$ (d), and $i = z$ (e). The average spin (polarization) of each is shown from the theoretical analysis (dashed blue line) and the simulations (solid black line, calculated from integrating the density along the s_i axis). The simulation parameters are the same as in Fig. 1.

$[\mathbf{s}(t_0)\cdot\mathbf{e}_\phi]\mathbf{e}_\phi = \cos\phi\mathbf{e}_\phi$ is the component parallel to $\mathbf{\Omega}$ and $\mathbf{s}_\perp(t_0) = \mathbf{s}(t_0) - \mathbf{s}_\parallel(t_0) = \sin\phi\mathbf{e}_r$ is the component perpendicular to $\mathbf{\Omega}$. One obtains the spin component along each axis from $s_x(t_0+\Delta T) = \mathbf{s}(t_0+\Delta T)\cdot\mathbf{e}_x = -\sin(\Delta\theta_s)\sin\phi$, $s_y(t_0+\Delta T) = \mathbf{s}(t_0+\Delta T)\cdot\mathbf{e}_y = \sin 2\phi(\cos\ \Delta\theta_s - 1)/2$, and $s_z(t_0+\Delta T) = \mathbf{s}(t_0+\Delta T)\cdot\mathbf{e}_z = \cos^2\phi + \sin^2\phi\cos\Delta\theta_s$. These results immediately reveal a key feature in wakefield acceleration: the spin distribution is a function of the coordinate angle ϕ. In the following, we show that the dependence holds for the beam polarization.

According to Refs. [38,40,50], the average fields in the plasma bubble take the form $E_r \approx cB_\phi \approx en(x)r/4\varepsilon_0$. Taking $\langle\beta_x\rangle \approx 1/2$, $\gamma \approx 1$, $\langle n(x)\rangle \approx (\alpha+1)n_0/2$, and $\langle r\rangle \approx r_i/2$ during the injection phase, one obtains $\langle\mathbf{\Omega}\rangle \approx -5e\langle B_\phi\rangle/4m \approx -5e^2(\alpha+1)n_0 r_i/64m\varepsilon_0$, tand hus $\Delta\theta_s \approx \langle\mathbf{\Omega}\rangle\Delta T \approx -\eta r_i|r_i|$, with $\eta = 5e^2(\alpha+1)n_0/16mc^2\varepsilon_0$. For simplicity, we assume a homogeneous electron distribution within the cylindrical injection volume of $|r_i| \le r_b(x_p)$ [27–29], where $r_b(x_p)$ is the bubble radius at the density peak, satisfying $r_b{}^2(x_p) \approx 4\sigma_l\sigma_r(n_{b0}/\alpha n_0)^{1/2}$ for PWFA [42,44] and $r_b{}^2(x_p) \approx 4amc^2\varepsilon_0/\alpha e^2 n_0$ for LWFA [51]. Therefore, combined with the fact that $\phi \approx \phi_p$, the polarization at certain ϕ_p becomes $d\zeta_i/d\phi_p \approx d\zeta_i/d\phi = \int_{-r_b(x_p)}^{r_b(x_p)} s_i|r|/r_b^2(x_p)dr$, where the three components ($i = x, y, z$) are

$$\frac{d\zeta_x}{d\phi_p} = \frac{1}{r_b^2(x_p)}\int_{-r_b(x_p)}^{r_{b(x_p)}} \sin(\eta r|r|)\sin\phi_p\,|r|dr = 0, \tag{4a}$$

$$\frac{d\zeta_y}{d\phi_p} = \frac{\sin 2\phi_p}{2r_b^2(x_p)}\int_{-r_b(x_p)}^{r_{b(x_p)}} [\cos(\eta r|r|) - 1]|r|dr = \frac{\sin 2\phi_p}{2}(\mathrm{sinc}\psi - 1), \tag{4b}$$

$$\frac{d\zeta_z}{d\phi_p} = \frac{1}{r_b^2(x_p)}\int_{-r_b(x_p)}^{r_b(x_p)} [\cos^2\phi_p + \sin^2\phi_p\cos(\eta r|r|)]|r|dr = 1 - \sin^2\phi_p(1 - \mathrm{sinc}\psi), \tag{4c}$$

where ψ is a normalized parameter denoting the largest precession angle under certain parameters; for example, $\psi = \eta r_b{}^2 = 5e^2(\alpha+1)\sigma_l\sigma_r(n_{b0}n_0)^{1/2}/4\alpha^{1/2}mc^2\varepsilon_0$ for PWFA and $\psi = 5a(\alpha+1)/4\alpha$ for LWFA. The spin distributions versus ϕ_p for the LWFA case are illustrated in Figs. 2(c)–2(e) ($\psi = 3.91$). The theoretical estimation from Eq. (4) shows good agreement with our simulations. Other cases, such as PWFA and LWFA driven by circularly polarized light, are also well described by Eq. (4).

Equation (4a) is confirmed by the simulation results in Figs. 1(c) and 2(c), where the polarization is close to 0 along the longitudinal axis (x axis). At any ϕ_p the spin values are antisymmetric around the $s_x = 0$ axis. Although the longitudinal component for each spin can be nonzero due to precession, a pair of centrally symmetric electrons precesses around opposite axes at the same frequency, resulting in opposite values of the longitudinal spin component. The polarization along the x axis naturally disappears in the statistic average. With regard to the s_y distribution, as exhibited in Figs. 1(d) and 2(d), the polarization peaks at $\phi_p = \pm\pi/4$. According to Eq. (4b), both $\mathbf{s}_\perp$ and $\mathbf{s}_\parallel$ contain a factor, $\sin(2\phi_p)/2$, that contributes to the y component, and the maximum absolute value (1–sinc ψ) is achieved at $\pi/4$.

The highest degree of polarization is preserved in the initial spin orientation. Equation (4c) clearly shows that the polarization along the z axis increases when $|\phi_p|$ is approaching zero, due to the $-\sin^2\phi_p$ term contributed by $\mathbf{s}_\perp$ and $\mathbf{s}_\parallel$. In particular, the polarization reaches 100% at $|\phi_p| \approx 0$ as illustrated in Fig. 2(e). This remarkable feature suggests an efficient method to maximize the beam polarization by selecting electrons around the phase-space angle ϕ_p.

We therefore propose the spin-filter approach to obtain electron bunches of high polarization purity. As sketched in Fig. 3(a), the driver beam excites a plasma wakefield in the prepolarized plasma target, which accelerates the injected electrons to high energies. After the acceleration, the electron beam can be filtered by an X-shaped slit. The spin distribution in the phase space is maintained over the long propagation distance after acceleration because the self-generated field of the electron beam still follows the form in Eq. (3). The slit is placed perpendicular to x with opening angle a_s so that electrons with ϕ_p satisfying $-\Delta\phi_p/2 \le \phi_p \le \Delta\phi_p/2$ ($\Delta\phi_p = \pi - a_s$) can pass and all other electrons are blocked. If we integrate Eqs. (4a)–(4c), we find the total polarization components $\zeta_i(\Delta\phi_p) = \int_{-\Delta\phi_p/2}^{\Delta\phi_p/2} d\zeta_i/\Delta\phi_p$ within the selected angular range:

$$\zeta_x(\Delta\phi_p) = \zeta_y(\Delta\phi_p) = 0, \tag{5}$$

$$\zeta_z(\Delta\phi_p) = \frac{1 + \mathrm{sinc}\ \Delta\phi_p}{2} + \frac{1 - \mathrm{sinc}\ \Delta\phi_p}{2}\mathrm{sinc}\psi. \tag{6}$$

Such spin filtering preserves the polarization only in the z direction (the prepolarized direction). As shown in Fig. 3(b), the simulation results for both LWFA and PWFA are in agreement with Eq. (5). The polarization decreases with larger values of $\Delta\phi_p$. To be specific, the polarization is 96% for LWFA and 98% for PWFA at $\Delta\phi_p = \pi/10$, while the polarization without the spin filter ($\Delta\phi_p = \pi$) is only 35% for LWFA and 49% for PWFA.

The spin-filter mechanism is universal in a large parameter range. The beam polarization as a function of the dimensionless parameter ψ is summarized in Fig. 3(c), for different parameter combinations. While, in general, smaller selecting angles induce high polarization purity,

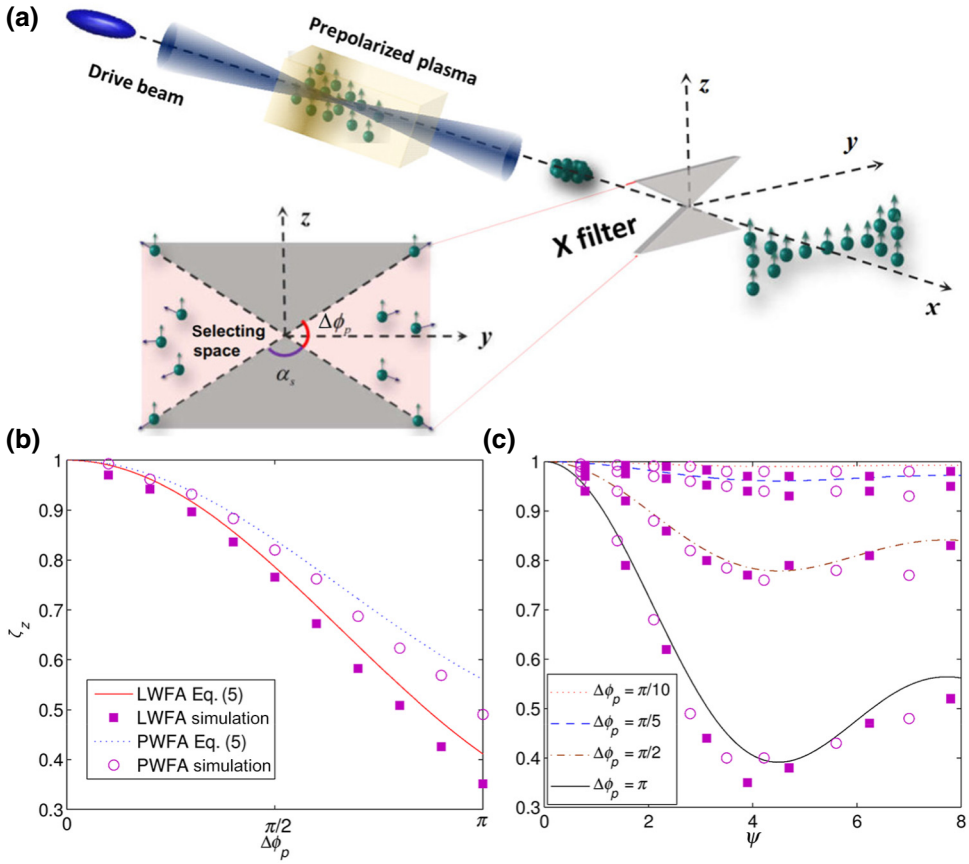

FIG. 3. (a) A spin filter using the X-shaped slit to produce polarized electron beams, where the slit selects electrons within the region $[-\Delta\phi_p/2,\ \Delta\phi_p/2]$. (b) Beam polarization along the z axis (ζ_z) as a function of the selecting angle $\Delta\phi_p$ for LWFA (solid red line and cyan squares) and PWFA (dotted blue line and cyan circles). The simulation results are obtained with the same parameters as in Fig. 2. (c) ζ_z as a function of the normalized parameter ψ from simulations for LWFA (cyan squares) and PWFA (cyan circles) with $\Delta\phi_p = \pi/10$, $\pi/5$, $\pi/2$, and π. The simulations results are given for $a = 0.5$–5 for LWFA and $\sigma_l = 0.8 \approx 4\ \mu$m, $\sigma_r = 1.6 \approx 3.2\ \mu$m, and $n_{b0} = 1.5\times10^{19}\ \mathrm{cm}^{-3}$ for PWFA with $\alpha = 4$ and $n_0 = 10^{18}\ \mathrm{cm}^{-3}$. The theoretical predictions are shown by lines.

we see that the beam polarization is already close to 80% for $\Delta\phi_p = \pi/2$ (90% for $\Delta\phi_p = \pi/5$ and $\pi/10$). In other words, the beam polarization is significantly purified by filtering out only half of the electron flux. Without spin filtering, the beam flux would be strongly restricted to preserve the polarization. As illustrated in Fig. 3(c), $\psi < 2$ is required to maintain a beam polarization greater than 80% when there is no filtering ($\Delta\phi_p = \pi$). Such restrictions disappear in our X-filter strategy. One can find from Fig. 3(c) that for a large value of ψ (representing the beam flux), the beam polarization after spin filtering $\Delta\phi_p \le \pi/2$ is greater than 80% throughout the full region.

An interesting phenomenon is that the polarization is not monotone with ψ. The z component of the spin $s_z = \cos^2\phi + \sin^2\phi\cos\Delta\theta_s$ oscillates with $\Delta\theta_s$, decreasing in the range $[2K\pi, (2K+1)\pi]$ and increasing in the range $[(2K+1)\pi, (2K+2)\pi]$, where K is an integer. The intrinsic nature of the spin-filter mechanism is attributed to the field geometry of the wakefield. For transverse initial polarization, the precession axis is along $\mathbf{e}_\phi$ and the rotation spin component $\mathbf{s}_\perp$ is anisotropic for different ϕ_p around the procession axis $\mathbf{e}_\phi$. As a consequence, the degree of spin precession depends on ϕ_p, which leads to a disparity of polarization in the transverse phase space. However, for longitudinal initial polarization, the rotation component is $|\boldsymbol{s}_\perp| = 1$ for all electrons, which means that the precession degree is independent of ϕ_p. We conclude that the spin-filter mechanism is not valid for the longitudinal case.

IV. DISCUSSION

The results shown above are based on an ideal situation, where the bubble is in perfect cylindrical symmetry, the plasma is cold initially, the drive beams are precisely aligned to the filter center, and the filter is treated ideally (the thickness is zero). However, in a real experiment, the bubble is usually not so perfectly symmetric, the plasma gains initially temperature from prepulses; the drive beams jitter for high-power laser systems and the filter has a finite size. This section is devoted to the robustness of our method against the imperfections.

To evaluate imperfect-plasma-wakefield effects (field asymmetry), we introduce two parameters (ρ_1, ρ_2) in the drive-beam profile in our 3D PIC simulations:

$$E_L = a[1+\rho_2\delta(y,z)]w_0^2/w^2(x)\sin^2(\pi t/2\tau_0)\sin(\pi r^2/\lambda R) \times \exp\{-[\rho_1 y^2 + (2-\rho 1)z^2)]/w^2(x)\}, \quad (7)$$

where $0 < \rho_1 < 2$ measures the ellipticity of the transverse intensity profile (perfectly circular for $\rho_1 = 1$) and $0 < \rho_2 < 1$ represents the degree of field fluctuation (zero fluctuation at $\rho_2 = 0$) multiplied by random numbers uniformly distributed at transverse coordinate $\delta(y,z)$ in the

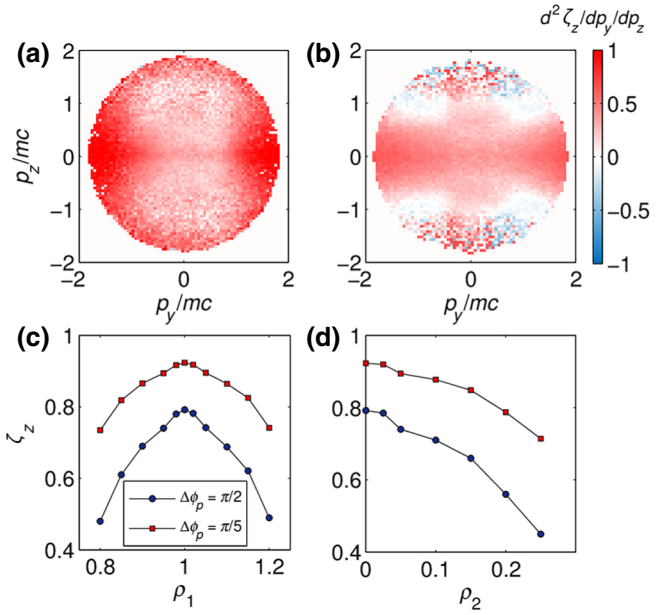

FIG. 4. Polarization (statistics along the z axis) distributions in the transverse phase space (p_y-p_z) for (a) $\rho_1 = 0.9$ and $\rho_2 = 0$ and (b) $\rho_1 = 0.8$ and $\rho_2 = 0$. The polarization along the z axis as a function of (c) ρ_1 and (d) ρ_2 for selecting angles $\Delta\phi_p = \pi/2$ and $\pi/5$. The other simulation parameters are the same as in Fig. 1.

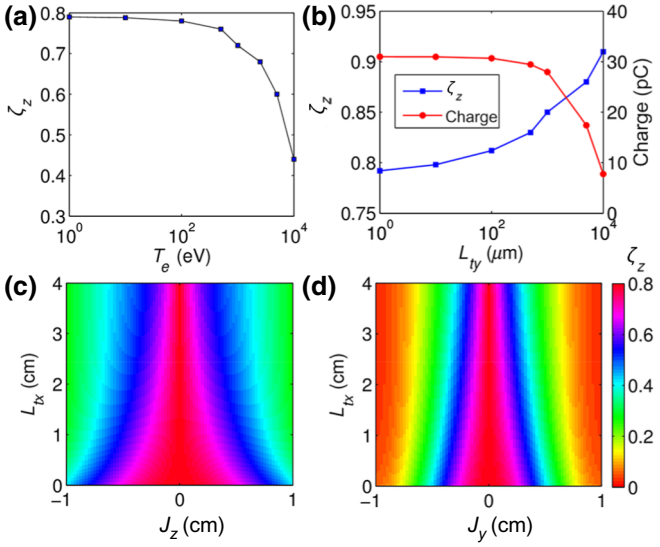

FIG. 5. (a) Polarization along the z axis as a function of initial electron temperature. (b) Polarization (blue squares) and selecting charge (red circles) as a function of the transverse size (along the y axis) of the filter L_{ty}. The polarization as a function of longitudinal thickness (along the x axis) L_{tx} and drive-beam jitter in the z direction ($j_y = 0$) (c) and in the y direction ($j_z = 0$) (d). The target is set 50 cm from the filter. The selecting angle $\Delta\phi = \pi/2$, while the other simulation parameters are the same as in Fig. 1.

range $[-1,1]$. The latter represents a type of quite harsh fluctuation that could possibly happen in experiments.

We first investigate the tolerance of ρ_1 (ρ_2 is set to 0). As shown in Figs. 4(a) and 4(b), for $\Delta\phi_p = \pi/2$ (50% filter) the angular dependence of the spin distribution is well preserved at $\rho_1 = 0.9$ but not so for $\rho_1 = 0.8$, where the polarization declines in the filter region due to mixing of the spins in the asymmetric field. From the scanning results depicted in Fig. 2(c), the polarization with $\Delta\phi_p = \pi/2$ is greater than 70% for $0.9 < \rho_1 < 1.1$, indicating a tolerable fluctuation within $\pm 10\%$ for ellipticity. It can be further relaxed to $\pm 20\%$ ($0.8 < \rho_1 < 1.2$) when a smaller filter is chosen, $\Delta\phi_p = \pi/5$. We then show the impacts of field fluctuation by setting $\rho_1 = 1$ and varying ρ_2 from 0 to 0.25. As illustrated in Fig. 4(d), the polarization declines due to the uneven distribution of the bubble field. Nevertheless, the polarization still surpasses 70% for $\rho_2 < 0.1$ when $\Delta\phi_p = \pi/2$ and $\rho_2 < 0.25$ when $\Delta\phi_p = \pi/5$. These results imply that about 20% fluctuation of the laser-field amplitude is tolerable for the filter mechanism.

As mentioned above, the plasma is not completely cold before arrival of the main pulse. Since the thermal motion of electrons affects the spin-filter process through the mapping from ϕ and ϕ_p, we perform simulations with different initial temperatures (assuming the electrons satisfy the Maxwell-Boltzmann distribution) for the same parameters as in Fig. 1. As illustrated in Fig. 5(a), the polarization is much greater than 70% for temperatures approaching 1 keV. This is fulfilled in typical wakefield-acceleration experiments.

In Sec. III, the filter is considered as an ideal plane without thickness. In reality, both the transverse size and the longitudinal thickness of our designed filter may affect the selecting polarization. These effects can be seen from Monte Carlo simulations, where the target is set 50 cm from the filter. When the transverse size L_{ty} of the filter increases, the polarization of the selecting beam is enhanced, while the total charge declines, as shown in Fig. 5(b). The polarization increases to about 90% when L_{ty} reaches 1 cm, whereas the charge of the selecting beam drops to about 8 pC. The filter thickness L_{tx} has a joint effect with the beam jitter on the selecting process. In simulations, we artificially introduce a position shift (along the y axis and the z axis) between the drive beam axis and the X-filter center. The thickness of the filter is also varied. The statistics are shown in Figs. 5(c) and 5(d). Here j_z and j_y represent the distance along y and z directions at the front plane of the filter between beam center and filter center. Not surprisingly, one finds the polarization declines with the augment of both jitter and longitudinal thickness. For thicker filters, the tolerant range of jitter is smaller. However, the polarization is much greater than 70% if the position jitter is less than 1 mm and $L_{tx} < 4$ cm. These results provide guidance for future experiments.

V. SUMMARY

In conclusion, we investigate the azimuthal dependence of the beam polarization in the wakefield and propose a spin-filter strategy for transversally polarized electron beams. By means of PIC simulations and theoretical analyses in the scope of a quasistatic model, we find that the precession degree varies for certain ϕ_p (the azimuthal angle in the phase space). In particular, electron spin directions are almost preserved during acceleration along the $\phi_p = 0$ axis ($\phi_p = \pi/2$ if initially polarized along the y axis) since the rotation components are vanishing. Therefore, applying this effect can maximize the beam polarization via selection of electrons in certain phase-space regions, at moderate cost of the beam flux. According to the theoretical model and 3D simulations, about 80% beam polarization can be obtained by filtering out half of all the electrons, compared with about 35% for the unfiltered beam. The robustness of the method is discussed for various imperfect situations, which will guide future experiments in high-power-laser facilities. The filtering mechanism is universal in a large parameter range. The limitations for the driver-beam parameters and the total beam flux are relieved, which hampered previous schemes. These highly polarized electron beams are advantageous in applications such as future electron-positron colliders.

ACKNOWLEDGMENTS

This work was supported by the Strategic Priority Research Program of the Chinese Academy of Sciences (Grant No. XDB 16010000), the National Natural Science Foundation of China (Grants No. 11875307 and No. 11935008), and the Recruitment Program for Young Professionals. M.B. and A.H. acknowledge support through the HGF-ATHENA project.

[1] T. Tajima and J. M. Dawson, Laser Electron Accelerator, Phys. Rev. Lett. **43**, 267 (1979).

[2] P. Chen, J. M. Dawson, R. W. Huff, and T. Katsouleas, Acceleration of Electrons by the Interaction of a Bunched Electron Beam with a Plasma, Phys. Rev. Lett. **54**, 693 (1985).

[3] E. Esarey, C. B. Schroeder, and W. P. Leemans, Physics of laser-driven plasma based electron accelerators, Rev. Mod. Phys. **81**, 1229 (2009).

[4] Alexander Wu Chao and Karl Hubert Mess, eds. *Handbook of Accelerator Physics and Engineering* (World scientific, Singapore, 2013).

[5] W. P. Leemans, B. Nagler, A. J. Gonsalves, Cs. Tóth, K. Nakamura, C. G. R. Geddes, E. Esarey, C. B. Schroeder, and S. M. Hooker, Gev electron beams from a centimetre-scale accelerator, Nat. Phys. **2**, 696 (2006).

[6] A. J. Gonsalves, et al., Petawatt Laser Guiding and Electron Beam Acceleration to 8 GeV in a LaserHeated Capillary Discharge Waveguide, Phys. Rev. Lett. **122**, 084801 (2019).

[7] W. P. Leemans, A. J. Gonsalves, H.-S. Mao, K. Nakamura, C. Benedetti, C. B. Schroeder, Cs. Tóth, J. Daniels, D E Mittelberger, S. S. Bulanov, J.-L. Vay, C. G. R. Geddes, and E. Esarey, Multi-GeV Electron Beams from Capillary-Discharge-Guided Subpetawatt Laser Pulses in the Self-Trapping Regime, Phys. Rev. Lett. **113**, 245002 (2014).

[8] Ian Blumenfeld, Christopher E. Clayton, Franz-Josef Decker, Mark J. Hogan, Chengkun Huang, Rasmus Ischebeck, Richard Iverson, Chandrashekhar Joshi, Thomas Katsouleas, Neil Kirby, Wei Lu, Kenneth A. Marsh, Warren B. Mori, Patric Muggli, Erdem Oz, Robert H. Siemann, Dieter Walz, and Miaomiao Zhou, Energy doubling of 42GeV electrons in a metre-scale plasma wakefield accelerator, Nature (London) **445**, 741 (2007).

[9] E. Adli, et al., Acceleration of electrons in the plasma wakefield of a proton bunch, Nature **561**, 363 (2018).

[10] A. Deng, et al., Generation and acceleration of electron bunches from a plasma photocathode, Nat. Phys. **15**, 1156 (2019).

[11] ALEGRO collaboration. Towards an Advanced Linear International Collider[J]. arXiv preprint arXiv:1901.10370, 2019.

[12] C. B. Schroeder, E. Esarey, C. G. R. Geddes, C. Benedetti, and W. P. Leemans, Physics considerations for laser-plasma linear colliders, Phys. Rev. Spec. Top. -Accel. Beams **13**, 101301 (2010).

[13] C. Bartels, M. Berggren, and J. List, Characterising WIMPs at a future e+ e− linear collider, Eur. Phys. J. C **72**, 2213 (2012).

[14] G. Moortgat-Pick, et al., Polarized positrons and electrons at the linear collider, Phys. Rep. **460**, 131 (2008).

[15] T. Hirose, K. Dobashi, Y. Kurihara, T. Mutob, T. Omorib, T. Okugib, I. Sakaia, J. Urakawab, and M. Washio, Polarized positron source for the linear collider, JLC, Nucl. Instrum. Methods Phys. Res. A **455**, 15 (2000).

[16] G. Moortgat-Pick, A. Bartl, H. Fraas, and W. Majerotto, Impact of e^+ and e^- beam polarization on chargino and neutralino production at a linear collider, Eur. Phys. J. C **18**, 379 (2000).

[17] R. Märtin, G. Weber, R. Barday, Y. Fritzsche, U. Spillmann, W. Chen, R. D. DuBois, J. Enders, M. Hegewald, S. Hess, A. Surzhykov, D. B. Thorn, S. Trotsenko, M. Wagner, D. F. A. Winters, V. A. Yerokhin, and Th. Stöhlker, Polarization Transfer of Bremsstrahlung Arising from Spin-Polarized Electrons, Phys. Rev. Lett. **108**, 264801 (2012).

[18] PEPPo Collaboration, Production of Highly Polarized Positrons Using Polarized Electrons at mev Energies, Phys. Rev. Lett. **116**, 214801 (2016).

[19] S. R. Mane, Y. M. Shatunov, and K. Yokoya, Spin-polarized charged particle beams in high-energy accelerators, Rep. Prog. Phys. **68**, 1997 (2005).

[20] Gay TJ. *Advances In Adv. Atom. Mol. Opt. Phys.*. Vol. 57 (Academic Press, New York, 2009), pp. 157–247.

[21] P. S. Farago, Electron spin polarization, Rep. Prog. Phys. **34**, 1055 (2002).

[22] A. A. Sokolov and I. M. Ternov, *Synchrotron Radiation* (Akademic, Germany, 1968).

[23] Yan-Fei Li, Rashid Shaisultanov, Karen Z. Hatsagortsyan, Feng Wan, Christoph H. Keitel, and Jian-Xing Li, Ultrarelativistic Electron-Beam Polarization in Single-Shot Interaction with an Ultraintense Laser Pulse, Phys. Rev. Lett. **122**, 154801 (2019).

[24] D. T. Pierce, F. Meier, and P. Zürcher, Negative electron affinity GaAs: A new source of spin-polarized electrons, Appl. Phys. Lett. **26**, 670 (1975).

[25] H. Batelaan, A. S. Green, B. A. Hitt, and T. J. Gay, Optically Pumped Electron Spin Filter, Phys. Rev. Lett. **82**, 4216 (1999).

[26] M. Dellweg M and C. Müller, Spin-polarizing Interferometric Beam Splitter for free Electrons, Phys. Rev. Lett. **118**, 070403 (2017).

[27] M. Wen, M. Tamburini, and H. Keitel C, Polarized Laser-Wakefield-Accelerated Kiloampere Electron Beams, Phys. Rev. Lett. **122**, 214801 (2019).

[28] Yitong Wu, Liangliang Ji, Xuesong Geng, Qin Yu, Nengwen Wang, Bo Feng, Zhao Guo, Weiqing Wang, Chengyu Qin, Xue Yan, Lingang Zhang, Johannes Thomas, Anna Hützen, Markus Büscher, T. Peter Rakitzis, Alexander Pukhov, Baifei Shen, and Ruxin Li, Polarized electron-beam acceleration driven by vortex laser pulses, New J. Phys. **21**, 073052 (2019).

[29] Yitong Wu, Liangliang Ji, Xuesong Geng, Qin Yu, Nengwen Wang, Bo Feng, Zhao Guo, Weiqing Wang, Chengyu Qin, Xue Yan, Lingang Zhang, Johannes Thomas, Anna Hützen, Alexander Pukhov, Markus Büscher, Baifei Shen, and Ruxin Li, Polarized electron beam generation in beam-driven plasma wakefield acceleration based on density tailing injection, Phys. Rev. E **100**, 043202 (2019).

[30] Dimitris Sofikitis, Luis Rubio-Lago, Lykourgos Bougas, Andrew J. Alexander, and T. Peter Rakitzis, Laser detection of spin-polarized hydrogen from HCl and HBr photodissociation: Comparison of H- and halogen-atom polarizations, J. Chem. Phys. **129**, 144302 (2008).

[31] T. P. Rakitzis, P. C. Samartzis, R. L. Toomes, T. N. Kitsopoulos, Alex Brown, G. G. Balint-Kurti, O. S. Vasyutinskii, and J. A. Beswick, Spin polarized hydrogen atoms from molecular photodissociation, Science **300**, 1936 (2003).

[32] P. Rakitzis T, Pulsed-laser production and detection of spin-polarized hydrogen atoms, Eur. J. Chem. Phys. Phys. Chem. **5**, 1489 (2004).

[33] D. Sofikitis, C. S. Kannis, G. K. Boulogiannis, and T. P. Rakitzis, Ultrahigh-Density Spin-Polarized H and D Observed via Magnetization Quantum Beats, Phys. Rev. Lett. **121**, 083001 (2018).

[34] Anna Hützen, Johannes Thomas, Jürgen Böker, Ralf Engels, Ralf Gebel, Andreas Lehrach, Alexander Pukhov, T. Peter Rakitzis, Dimitris Sofikitis, and Markus Büscher, Polarized proton beams from laser-induced plasmas, High Power Laser Sci **7**, E16 (2019).

[35] A. Pukhov, Particle-In-Cell codes for plasma-based particle acceleration, CERN Yellow Reports **1**, 181 (2016).

[36] V. Bargmann, L. Michel, and V. L. Telegdi, Precession of the Polarization of Particles Moving in a Homogeneous Electromagnetic Field, Phys. Rev. Lett. **2**, 435 (1959).

[37] M. Wen, C. H. Keitel, and H. Bauke, Spin-one-half particles in strong electromagnetic fields: Spin effects and radiation reaction, Phys. Rev. A **95**, 042102 (2017).

[38] R. M. Kulsrud, H. P. Furth, E. J. Valeo, and M. Goldhaber, Fusion Reactor Plasmas with Polarized Nuclei, Phys. Rev. Lett. **49**, 1248 (1982).

[39] K. Schmid, A. Buck, C. M. S. Sears, J. M. Mikhailova, R. Tautz, D. Herrmann, M. Geissler, F. Krausz, and L. Veisz, Density-transition based electron injector for laser driven wakefield accelerators, Phys. Rev. Spec. Top. Accel. Beams **13**, 091301 (2010).

[40] A. Buck, J. Wenz, J. Xu, K. Khrennikov, K. Schmid, M. Heigoldt, J. M. Mikhailova, M. Geissler, B. Shen, F. Krausz, S. Karsch, and L. Veisz, Shock-Front Injector for High-Quality Laser-Plasma Acceleration, Phys. Rev. Lett. **110**, 185006 (2013).

[41] A. J. Gonsalves, K. Nakamura, C. Lin, D. Panasenko, S. Shiraishi, T. Sokollik, C. Benedetti, C. B. Schroeder, C. G. R. Geddes, J. van Tilborg, J. Osterhoff, E. Esarey, C. Toth, and W. P. Leemans, Tunable laser plasma accelerator based on longitudinal density tailoring, Nat. Phys. **7**, 862 (2011).

[42] A. Golovanov A, I. Yu Kostyukov, J. Thomas, and A. Pukhov, Analytic model for electromagnetic fields in the bubble regime of plasma wakefield in non-uniform plasmas, Phys. Plasmas **24**, 103104 (2017).

[43] N. E. Andreev, L. M. Gorbunov, V. I. Kirsanov, K. Nakajima, and A. Ogata, Structure of the wake field in plasma channels, Phys. Plasmas **4**, 1145 (1997).

[44] K. V. Lotov, Blowout regimes of plasma wakefield acceleration, Phys. Rev. E **69**, 046405 (2004).

[45] J. Vieira, C.-K. Huang, W. B. Mori, and L. O. Silva, Polarized beam conditioning in plasma based acceleration, Phys. Rev. **14**, 071303 (2011).

[46] X. L. Xu, F. Li, W. An, T. N. Dalichaouch, P. Yu, W. Lu, C. Joshi, and W. B. Mori, High quality electron bunch generation using a longitudinal density-tailored plasma-based accelerator in the three-dimensional blowout regime, Phys. Rev. **20**, 111303 (2017).

[47] S. Kalmykov, A. Beck, S. A. Yi, V. Khudik, M. C. Downer, E. Lefebvre, B. A. Shadwick, and D. P. Umstadter, Electron selfinjection into an evolving plasma bubble: Quasi-monoenergetic laser-plasma acceleration in the blowout regime, Phys. Plasmas **18**, 056704 (2011).

[48] S. Kalmykov, S. A. Yi, V. Khudik, and G. Shvets, Electron Self-injection and Trapping into an Evolving Plasma Bubble, Phys. Rev. Lett. **103**, 135004 (2009).

[49] K. Swanson, H.-E. Tsai, S. Barber, R. Lehe, H.-S. Mao, S. Steinke, J. V. Tilborg, C. G. R. Geddes, and W. P. Leemans. Electron beam control using shock-induced density downramp injection, in Advanced Accelerator Cconcepts: 17th Advanced Accelerator Concepts Workshop, edited by S. H. Gold, G. S. Nusinovich, and K. P. Wootton, AIP Conf. Proc. No. 1812 (AIP, Melville, New York, 2017), p. 040004.

[50] I. Kostyukov, A. Pukhov, and S. Kiselev, Phenomenological theory of laser-plasma interaction in 'bubble' regime, Phys. Plasmas **11**, 5256 (2004).

[51] W. Lu, M. Tzoufras, C. Joshi, F. S. Tsung, W. B. Mori, J. Vieira, R. A. Fonseca, and L. O. Silva, Generating multi-gev electron bunches using single stage laser wakefield acceleration in a 3d nonlinear regime, Phys. Rev. ST Accel. Beams **10**, 061301 (2007).